Shaking Table Tests and Numerical Analysis of the Interaction of a Base-isolated Steel Frame's Responses with a Long-span Roof

Tianyang Zhang [a], **Haoru Guo**[a], **Yunlong Zhang** [a], **Weizhi Xu** [a,b], **Shuguang Wang**[a], **and Dongsheng Du**[a]

[a]College of Civil Engineering, Nanjing Tech University, Nanjing 211816, China
[b]China-Pakistan Belt and Road Joint Laboratory on Smart Disaster Prevention of Major Infrastructures, Southeast University, Nanjing 210096, China

ABSTRACT

Seismic isolation technology has been extensively used in long-span spatial structures to alleviate losses caused by earthquake disasters. However, limited experimental studies have been conducted to examine the impact of horizontal and vertical vibrations in long-span roof structures with rubber bearings as isolation layers on the isolation effect. This paper presents a study that carried out shaking table experiments on 1/40 scale long-span steel frames, both with and without base isolation. It explores the interplay of horizontal and vertical vibrations in long-span roof structures equipped with rubber bearings, and its influence on the isolation effect. Three ground motions, including horizontal bidirectional (2D) and bidirectional-plus-vertical (3D) components were used as the seismic excitations. The whole structural dynamic responses of the base-isolation (BI) model and fixed-base (FB) model, the local responses of the grids and isolation bearings were measured. Under 2D seismic excitation, the grid layer in the FB model exhibits a substantial vertical acceleration response. When exposed to 3D seismic activity, the isolation system successfully delivers its expected isolation outcome. Although the isolation bearings could not attenuate the vertical seismic acceleration response induced by vertical ground motion, they effectively reduced the vertical dynamic response generated by the coupling by suppressing the horizontal seismic response.

1. Introduction

As the main form of public buildings, long-span spatial structures are widely used in stadiums, airports and exhibition buildings. The long-span spatial structures have the characteristics of dense population flow, high importance and complex shape (Ding et al., 2019). Additionally, the long-span structures have obvious spatial stress characteristics. Most of these structures are flexible with a large period and low damping, which are sensitive to dynamic action and prone to strength failure (Tubino et al., 2003). Isolation technology has been tested and theoretically verified to effectively mitigate seismic damage to building structures (Zhu et al., 2014). Xue et al. (2010) proposed a novel three-dimensional composite seismic isolator that used frictional sliding isolation for horizontal motion and helical spring or disc spring for vertical motion. The results of the shaking table test showed

that the newly developed isolator had excellent seismic isolation performance, significantly prolonged the period of the isolated structure, and reduced the peak axial force amplitude by more than 50%. Ding et al. (2011) proposed a streamlined design approach for long-span structures equipped with SMA isolators, and conducted a Finite Element Method (FEM) analysis. The analysis revealed that the SMA isolator effectively mitigates the seismic responses of the structure, thereby demonstrating the efficacy of the proposed SMA isolation technique. As a result, isolation technology, which involves the insertion of a flexible mechanical device to separate the structure from the source of vibration, has found extensive application in long-span spatial structures.

In the past two decades, numerous long-span spatial structure projects have been constructed worldwide, and many of them have applied isolation bearings to significantly reduce the seismic

🦋 Springer

response of the roof (Takeuchi et al., 2006). Typically, many airport terminal structures adopt base isolation. The terminal building of San Francisco International Airport in the United States has a hall with an area of 700×200 feet and a height of 94 feet. A total of 267 friction pendulum bearings were installed on the base of this landmark building, and the seismic performance target was set to no structural damage under an earthquake of magnitude 8 (Victor and Stanley, 2000). The terminal building of Beijing Daxing International New Airport, recognized as the world's largest single isolated structure, utilizes a combined isolation approach. The isolation layer of this structure comprises 1152 seismic isolation bearings, which include lead rubber bearings (LRBs), natural rubber bearings (NRBs), and elastic slide bearings, in addition to 160 linear viscous dampers. Shu et al. (2016) analysed the isolation effect of Beijing Daxing International New Airport. The results showed that the horizontal seismic decrease coefficient of each layer was less than 0.4 after isolation and met the specified design objectives. Hu et al. (2016) thoroughly explored the key points and design basis of various steps in the isolation layer design process, and formed the operational process that can guide the design.

The existing research on the large-span isolation structure focuses mainly on the horizontal isolated performance. However, the actual ground motion contains a significant vertical component. Under high-intensity ground motion, the damage caused by vertical vibration cannot be ignored. Papazoglou and Elnashai (1996) sorted out the observational data of three earthquakes, evaluated the failure modes of buildings and bridges caused by high vertical seismic force, and confirmed the influence of vertical motion. Kunnath et al. (2008) found, through the simulation analysis of long-span structures, that under the action of the vertical component of ground motion, the axial force demand of columns and the bending moment demand of beams were significantly enlarged. In addition to structural components, vertical ground motion can cause damage to nonstructural components. By shaking table tests of a full-scale five-story frame structure, Ryan and Dao (2012a) found that nonstructural components such as ceilings were damaged significantly under three-dimensional vibration compared with two-dimensional input. Yoshiro et al. (2008) recorded damage to the ceiling in the 2008 Yamada earthquake in Japan. The sensor recorded the obvious vertical vibration, and the ceiling and lamp in the stadium fell in large areas. The long-span grid structure had a large span, which produced a large internal force and deformation under vertical earthquakes, and the grid part is usually equipped with nonstructural components that are sensitive to vertical vibration. Therefore, the influence of vertical excitation should be considered.

The horizontal response of a structure is influenced not only by the horizontal seismic component but also by the vertical seismic component. Previous experimental studies have documented instances of coupling between the system's horizontal response and vertical ground excitation. However, the magnitude of the impact is not clear. Griffith (1988) noticed that the acceleration of the horizontal floor slightly increased (5% to 11%) in the case of a vertical input earthquake in the scaled shaking table test of a 6-storey concrete structure and a 9-storey steel frame with isolation bearings. Hwang and Hsu (2000) carried out scale tests on a three-storey steel structure with lead-rubber and natural rubber bearings, considering one-way, two-way and three-way seismic inputs. The acceleration of the upper structure's horizontal floor was markedly amplified by the vertical ground acceleration. Ryan and Dao (2012a) found that the peak roof horizontal acceleration of an isolated structure under three-dimensional seismic input is twice the peak roof horizontal acceleration under two-dimensional seismic input. Anand and Kumar (2018) have systematically summarized the latest research advancements in the field of Seismic Soil-Structure Interaction (SSI). The study points out that based on the stiffness comparison between the structure and the soil, SSI may vary, which can be beneficial or detrimental to the structural response during seismic events. Although the actual response is a function of frequency, depending on the seismic acceleration, it can be determined that rigid structures and heavy buildings established on soft soil are most severely affected. Contemporary research in the SSI field mainly focuses on exploring its impact on a certain type of structure or finding the principles behind its influence on general structural configurations, including strength reduction factor, ductility demand and modal characteristics.

To explore the influence of rubber bearings on the vertical response of isolated structures, shaking table tests were carried out by some scholars. Furukawa et al. (2013) conducted a full-scale shaking table test of a four-storey hospital model with rubber bearings. The vertical acceleration recorded in the test was significantly amplified compared with the input. Lu et al. (2011) conducted a scaled shaking table test of an airport terminal building and found that the vertical acceleration was amplified by 10% after passing through the isolation layer. The results of shaking table tests imply that rubber isolation bearings have no control effect on the vertical component of ground motion. Currently, research on vertical vibration control is focused mainly on the research and development of three-dimensional isolation bearings, and a three-dimensional isolation system is being developed for nuclear power plants and multistorey buildings (Ryan and Warn, 2012b). Huffmann (1985) installed the GERB three-dimensional isolation system on a five-storey steel frame model for shaking table tests. The results show that the vertical isolation effect is better, but the horizontal effect is not as good as the horizontal effect of a typical horizontal isolation bearing. The three-dimensional isolation scheme developed by Shimizu Corporation (Takahashi et al., 2008a, 2008b), which is realized by the three-dimensional isolation bearing and oil damper system, is suitable for civil buildings and other fields after full-scale tests, but the system is very complex and expensive.

Research on large-span isolation structures in existing engineering focuses on the horizontal isolation effect. Some test results show that the vertical vibration is amplified in the isolation layer, but less attention is given to the vertical control effect of the grid. Mazza and Vulcano (2012), Mazza et al. (2017, 2018) pointed out that the near-fault earthquakes are characterized by high

values of the ratio between the peak of vertical and horizontal ground accelerations thus tend to exhibit higher nonlinear response, which can significantly increase the horizontal-vertical coupling. A few studies have found the existence of horizontal and vertical coupling in isolated structures. Although the Chinese code (2010) requires supplementary calculation for the vertical seismic action of long-span roof structures under multidimensional earthquakes, the amplification of coupling is not considered in the analysis process. Large-span structures are sensitive to vertical seismic response due to the presence of their large-span roofs. Considering the interaction of reactions caused by horizontal and vertical excitations is important for the arrangement of non-structural components of large-span structures. Examining the interaction of horizontal and vertical dynamic responses in long-span spatial structures is a topic of interest. While there have been investigations into the horizontal-vertical coupling in multi-story or high-rise base-isolated structures, there is a noticeable scarcity of experimental studies on these coupling effects in large-span isolated structures when subjected to 3D seismic excitations. The objective of this study is to explore the seismic behavior of long-span isolated structures in areas of high seismic intensity area, taking into account the horizontal-vertical interaction via multi-dimensional shaking table experiments. For the purpose of the experiment, models with and without seismic isolation were created. The experimental program including test model design, instrumentation and input ground motions are described in section 2.

2. Experimental Program

2.1 Test Model

2.1.1 Brief Description of Prototype Structure
To study the coupling effect between horizontal and vertical dynamic reactions under earthquake, a prototypical fixed-base (FB) structure was conceived. This structure, a long-span grid roof spanning 108 m, serves as our primary model. As depicted in Fig. 1, this FB model comprises a standard steel frame floor and an expansive flat grid formation. The model's planar dimensions measure 108 m × 108 m. For the prototype structure, the box column sections of peripheral supporting columns and internal columns are, respectively, 1,600 mm × 100 mm (side length × thickness) and 800 mm × 40 mm. Considering the importance of large-span buildings in practical application, the seismic performance goal of the prototype structure was to maintain elasticity under earthquakes, and relatively weak nonlinearity under rare earthquakes to ensure that

the structure has sufficient safety redundancy. In order to make safety taking into account of the effects of extreme or unexpected seismic load conditions, base isolation technology is already applied in many building structures. The design horizontal period of the prototype FB structure is 0.72 s, and the target isolation period of the prototype base-isolated (BI) structure was designed to increase to more than 2 times that of FB structure in frequent earthquake, and 1.64 s was determined. Built as the BI structure, 49 rubber bearings consist of 16 LRB1200s, 16 LRB1300s and 17 NRB1300s, were placed under the peripheral supporting columns and internal columns of the base-fixed structure, respectively.

2.1.2 Simplified Design of Superstructure Model
Prior to detailing the model, it's essential to establish a similarity relationship in accordance with the theory of similarity. Given the geometric size constraints and load capacity of the shaking table, a length scaling ratio of 1:40 was initially set. The test model employed standard building steel, akin to the prototype, resulting in a 1:1 scaling ratio for Young's Modulus. As the research was primarily concerned with vertical seismic response, an acceleration scaling ratio of 1:1 was adopted to negate any gravitational distortion. Subsequently, other similarity coefficients can be determined according to the similitude laws, and the main similarity coefficients were listed in Table 1.

Constructed as a 1/40 scale replica of the intended prototype structure, the two-storey steel model was devised with a reach of 2,700 mm extending in two orthogonal horizontal directions, as illustrated in Fig. 2. The experimental model assembly method is shown in Fig. 2(a). The main cross sections of the anti-lateral force components, namely, the frame column, of the experimental model were determined according to the similarity ratio. The sections of some H-shaped prototype beam members were replaced by a square steel tube whose section moment of inertia and section area are as close as possible. The cross section information of the main structural members for the scaling model are listed in Table 2.

Given the complexity of the prototype roof structure, its numerous components, and the diminutive scale factor, it was imperative to simplify the scaled roof model. As the research primarily concentrated on the vertical dynamic response of the grid roof, it was crucial to design the grid roof judiciously to
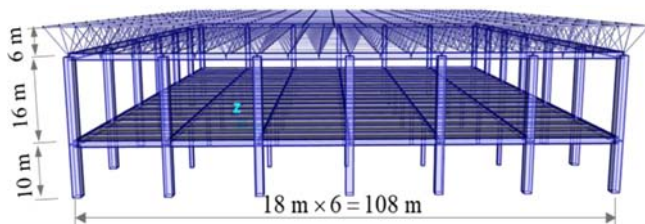

Fig. 1. View of Prototype FB Structure

Table 1. The Model-Prototype Similarity Coefficients

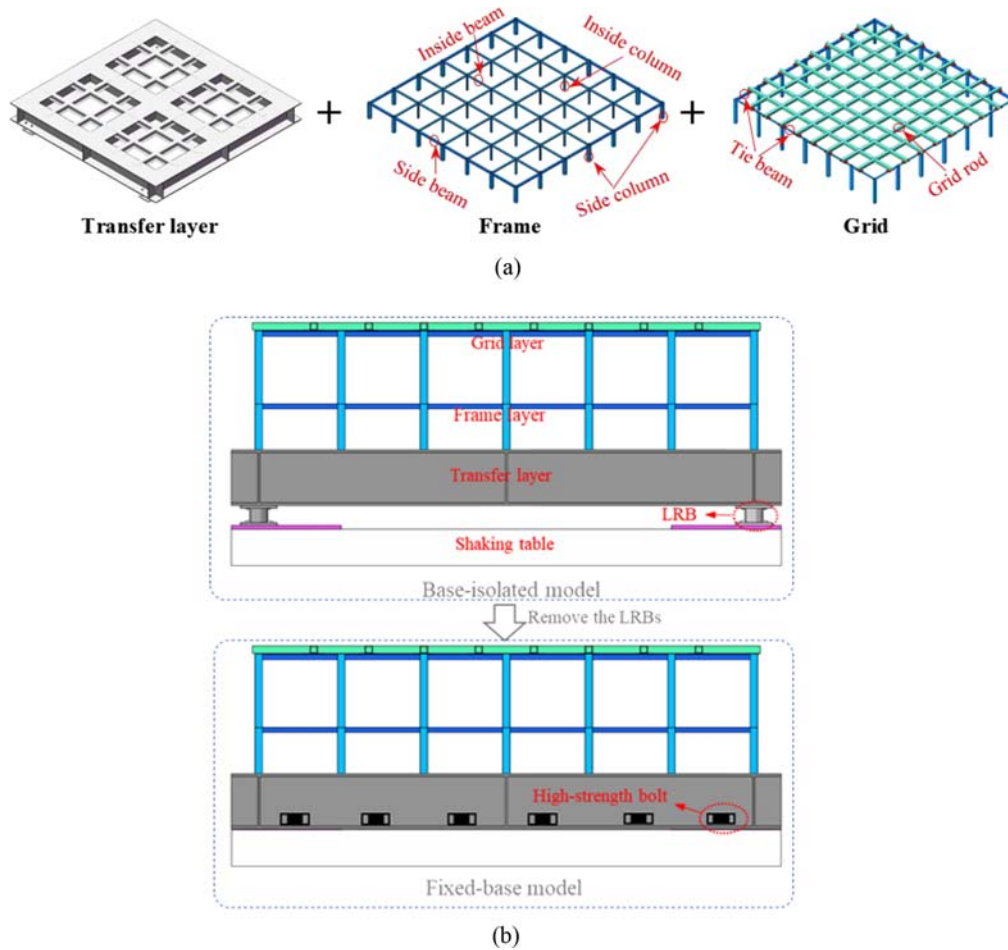| Physical Parameter	Similarity Relation	Scale coefficients
Length l	S_l	1:40
Young's Modulus E	S_E	1:1
Acceleration a	S_a	1:1
Mass m	$S_M = S_E S_l^2 S_a^{-1}$	1:1600
Stress σ	$S_\sigma = S_E$	1:1
Force F	$S_F = S_\sigma S_l^2$	1:1600
Stiffness k	$S_k = S_E S_l$	1:40
Damping Ratio ξ	S_ξ	1:1
Time/Period t	$S_t = S_l^{-0.5} / S_a^{0.5}$	1:6.325

Fig. 2. Details of Model Construction: (a) Superstructure Model Assembly, (b) Elevation of FB and BI Models

Table 2. Section Information of Components

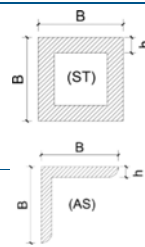| Location		Shape	B (mm)	h (mm)	Example
Frame	Side column	ST	40	2.5	
	Inside column	ST	20	1	
	Side beam	ST	25	2	
	Inside Beam	ST	20	1	
Roof	Grid rod	ST	40	2.5	
	Tie beam	AS	30	1.2	

Fig. 3. Plan View of Prototype Roof and Scaling Roof Model

guarantee the roof model possessed the appropriate vertical stiffness. The fundamental vertical vibration period and vertical deformation of seven controlling points (CPs) for the prototype roof structure and scaling roof model nodes (see Fig. 3) were analysed by Structural analysis software (Computer & Structures Inc, 2015) to evaluate the rationality of model simplification. The roof model exhibits a vertical vibration period of 0.138 s, while the prototype roof structure has a period of 0.827 s, respectively, and the ratio is 0.1669, which is very close to the design value of 0.1581. The vertical deflection of the seven CPs caused by

vertical static load are presented in Table 3. The discrepancy between the vertical deflection ratio of the model and the prototype, as well as the similarity ratio, is primarily within 10%. This affirms the suitability of the scaling model's vertical stiffness. The test model's equivalent floor mass was computed using the self-weight of the prototype structure and an additional floor load, in accordance with the similarity relationship. The mass distribution was adjusted by applying the counterweight block. The quality changes caused by grid simplification are compensated by distributing weights at nodes.

Table 3. Vertical Deflection of the Control Points for the Roof Structure

Control point	Vertical deflection (mm)		Ratio	Error
	Prototype structure	Model structure		
CP1	97.79	2.63	37.18	7.05%
CP2	191.21	4.80	39.84	0.40%
CP3	262.24	6.32	41.49	3.73%
CP4	300.19	7.09	42.34	5.85%
CP5	229.46	5.62	40.83	2.08%
CP6	123.30	3.23	38.17	4.58%
CP7	33.44	0.92	36.35	9.13%

Fig. 5. General View of Experimental Model

2.1.3 Design of Isolation Layer

The BI model adopts base isolation, as shown in Fig. 2(b). In the prototype structure, every frame at the base is fitted with isolation bearings. These bearings support a relatively lightweight superstructure, weighing approximately 1,917,000 kN. This results in an average axial load of about 3,912 kN per isolator when they are positioned under all columns. The total yield-force and post-yielding stiffness amount to 13,183 kN and 102,067 kN/m, respectively. Considering the equivalent total horizontal stiffness and total yield force of the isolation layer, the test model's isolation layer was reduced to four lead rubber bearings (LRBs), which were positioned at the four corners of the isolation layer. The base of the FB model was fixed. Compared with the BI model, the LRBs were removed, and the bottom frame was rigidly connected. To ensure that the seismic excitation can be effectively transmitted to the upper structure through the platform and the isolation layer, the transfer layer was set at the bottom of the structure. Steel beams HW300 × 300 × 10 × 15 and I100 were selected to make the transfer layer, which has sufficient vertical stiffness and sufficient horizontal stiffness to transmit seismic excitation. Fig. 4 illustrates the specifics of the LRB utilized in the test. The steel plate has an outer diameter of 100 mm and a thickness of 2 mm. The isolation layer comprises 16 rubber layers, each with a thickness of 1.2 mm. The lead core and connection plate have diameters of 14 mm and 20 mm, respectively. The overall height of the LRB is 119.2 mm. According to the People's Republic of China for Quality Supervision

and Inspection and Quarantine (2007), the basic mechanical properties of the isolation bearing used in the test were tested to detect its vertical stiffness and horizontal stiffness. After testing and calculation, the average yield force of the selected four isolation bearings is 2.05 kN, the average stiffness before yielding is 7.32 kN/mm, the average stiffness after yielding is 0.33 kN/mm, the average equivalent shear stiffness is 0.46 kN/mm, and the average compression stiffness is 251.05 kN/mm.

2.2 Instrument

Three-dimensional shaking table tests were conducted using an MTS Crop. Production with a 3 m × 3 m platform. A comprehensive view of the experimental model positioned on the shaking table can be observed in Fig. 5. To obtain the local and global response of the model, 40 acceleration sensors produced by Bruel & Kjaer S & V Measurement A/S in Denmark and 4 laser displacement sensors produced by OMRON Corporation in Japan were installed on the test model. Acceleration sensors were affixed to the shaking table, the apex of the side column, and the top grid node. Displacement sensors were positioned on both sides of the transfer layer. Both types of sensors were symmetrically distributed in the X- and Y- directions. The acceleration sensors, located on the model's side, served to track the horizontal dynamic response. Acceleration sensors, positioned on the top grid nodes, primarily function to track the vertical dynamic response. The displacement sensors, primarily tasked with quantifying the horizontal deformation of the isolation layer, were also installed. Strain gauges were
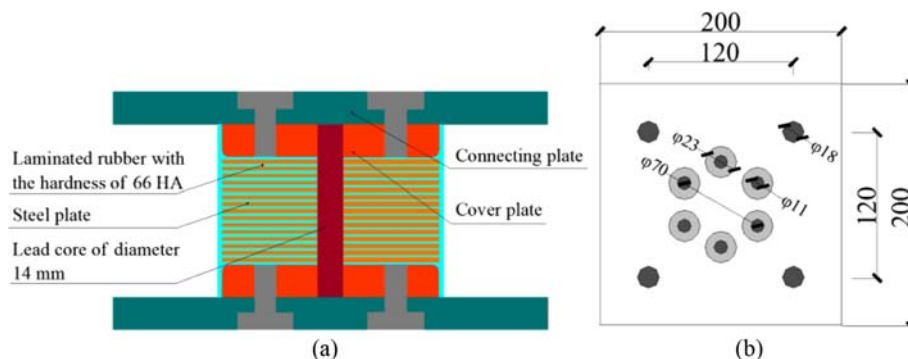
Fig. 4. LRB Configuration (Dimensions in mm): (a) Section View, (b) Vertical View
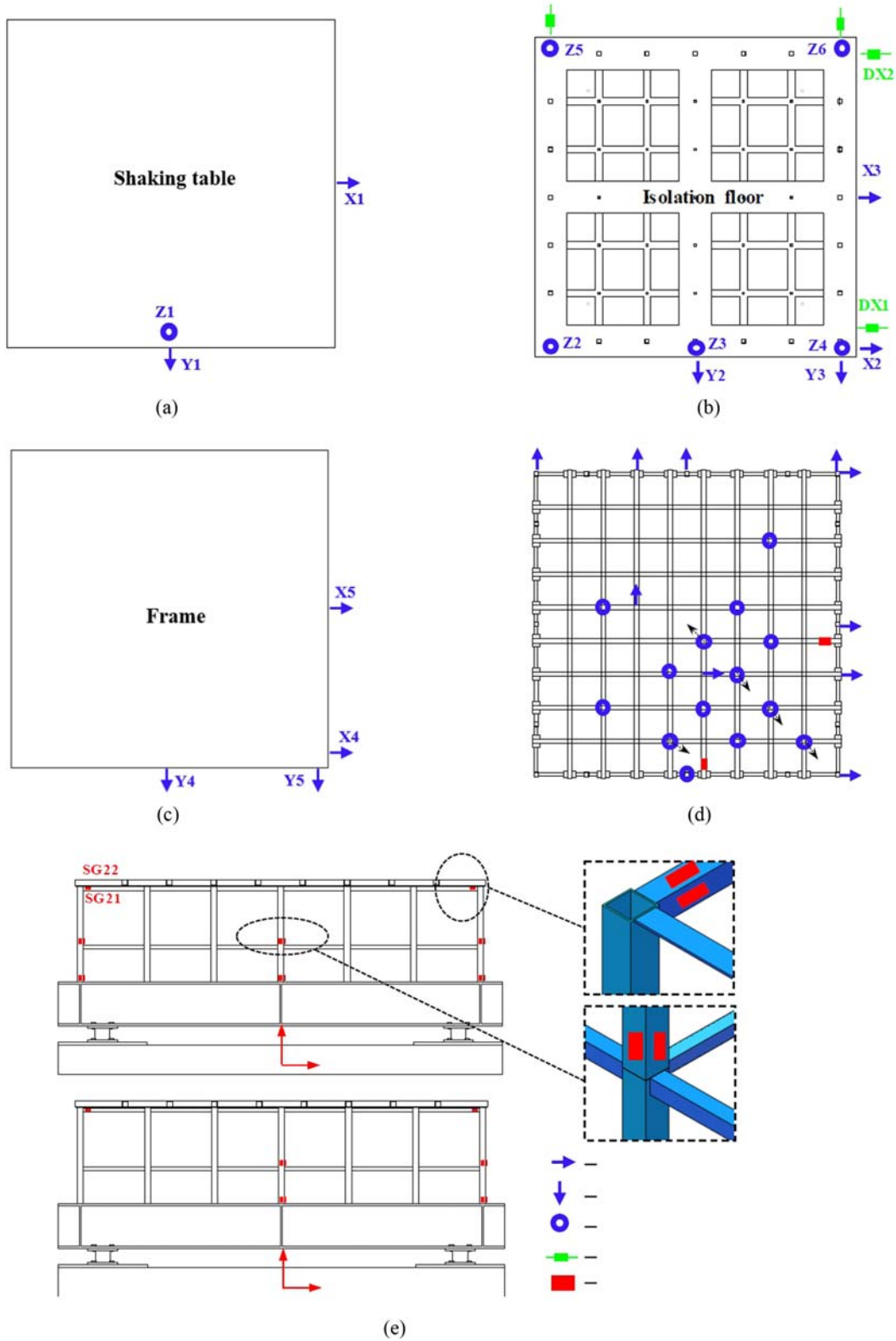
Fig. 6. Arrangement of Measuring Points: (a) Shaking Table, (b) Transfer Layer, (c) Frame Layer, (d) Grid Layer, (e) YZ and XZ Elevation

affixed to the base of each column, the extremity of the top beam, and selected bars of the grid roof. A comprehensive layout of the measurement points can be found in Fig. 6.

2.3 Input Ground Motions

Since the loading protocol of the shaking table tests was determined, different seismic waves and different seismic intensities were considered. Two typical natural seismic waves and an artificial

Table 4. Details of Ground Motions

Wave	Date	Location	Station	Duration (s)	Time interval (s)
El Centro	1940.05.19	Imperial Valley	El Centro Array #9	53.44	0.02
Taft	1952.07.21	Kern County	Taft Lincoln School	54.34	0.02
Artificial	/	/	/	59.94	0.02
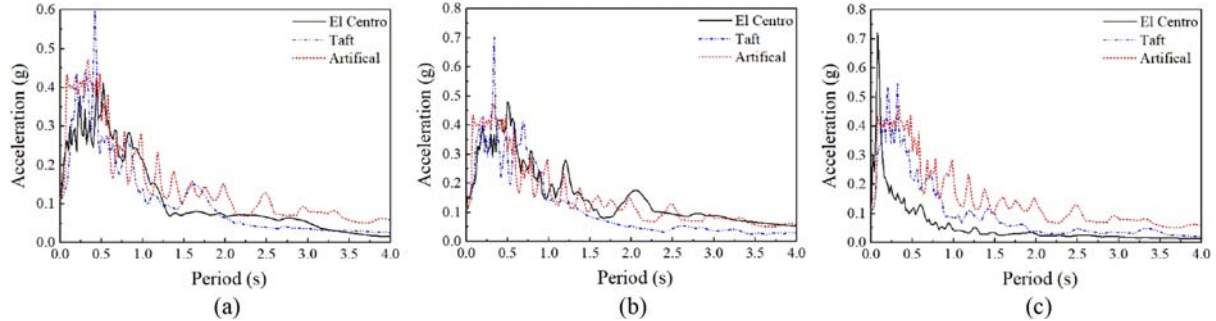
Fig. 7. Acceleration Response Spectra for 2% Damping in Horizontal and Vertical Directions: (a) X-Direction, (b) Y-Direction, (c) Z-Direction

wave, as shown in Table 4, were selected for simulated seismic input. The frequency-dependent power spectra density function, $S(\omega)$, proposed by Clough and Penzien (1975) was adopted in generating the ground motion. The parameters used in the equation were determined according to the Site condition and Standard acceleration response spectrum.

$$S(\omega) = \frac{\omega_g^4 + 4\varsigma_g^2\omega_g^2\omega^2}{(\omega_g^2 - \omega^2)^2 + 4\varsigma_g^2\omega_g^2\omega^2} \cdot \frac{\omega^4}{(\omega_f^2 - \omega^2)^2 + 4\varsigma_f^2\omega_f^2\omega^2} \cdot S_0 , \quad (1)$$

where ω is circular frequency, S_0 is intensity factor of power spectra density function; ς_g and ω_g are the damping ratio and circular frequency of local site soil, respectively; ς_f and ω_f are the factors for producing the desired filtering of the very low frequencies.

Figure 7 shows response spectra of input accelerations on the shaking table in three directions with peak ground acceleration (PGA) of 110 cm/s². The time interval of the acceleration time

history used as the seismic input of the shaking table tests is compressed according to the time similarity ratio of 0.1581. The BI model and FB model were subjected to 2D input and 3D input, respectively. Among them, horizontal loading only inputs ground motion in the X- and Y-directions, and three-dimensional loading also inputs ground motion in the Z-direction. According to China Ministry of Housing and Urban-Rural Development (2010), the vertical standard acceleration spectrum takes 0.65 times the horizontal standard acceleration spectrum. In addition, several existing shaking table test used same component in each direction (Jung et al., 2022). In this study, the authors also want to observe the amplification effect because of the use of same component. Hence, an artificial earthquake, maintaining uniform components in all directions, was employed for the shaking table experiments. Both models are subjected to 8-degree frequent earthquakes (F-XY and F-XYZ), 8-degree occasional earthquakes (O-XY and O-XYZ) and 8-degree rare earthquakes (R-XY and R-XYZ).

Table 5. Design of the Shaking-Table Test

Intensity	Input mode	Condition	PGA (g) at each direction		
			X	Y	Z
-	White noise	W1-X, W1-Y, W1-Z	0.1	0.1	0.1
Frequent	2D input	F-E-XY, F-T-XY, F-A-XY	0.11	0.0935	
	3D input	F-E-XYZ, F-T-XYZ, F-A-XYZ	0.11	0.0935	0.0715
-	White noise	W2-X, W2-Y, W2-Z	0.1	0.1	0.1
Occasional	2D input	O-E-XY, O-T-XY, O-A-XY	0.3	0.255	
	3D input	O-E-XYZ, O-T-XYZ, O-A-XYZ	0.3	0.255	0.195
-	White noise	W3-X, W3-Y, W3-Z	0.1	0.1	0.1
Rare	2D input	R-E-XY, R-T-XY, R-A-XY	0.51	0.4335	
	3D input	R-E-XYZ, R-T-XYZ, R-A-XYZ	0.51	0.4335	0.3315
-	White noise	W4-X, W4-Y, W4-Z	0.1	0.1	0.1

Note: "E" represents the El Centro wave, "T" represents the Taft wave, "A" represents the artificial wave

During the tests under seismic input, white noise excitations in the X-, Y- and Z-directions were applied in sequence before and after each earthquake intensity level, and dynamic characteristic parameters such as the natural frequency and damping ratio of the test model were obtained from the captured acceleration response data, further details about dynamic characteristics are given in Section 3. A total of 30 loading cases were conducted in the order given in Table 5.

3. Dynamic Characteristics

Dynamic characteristics including natural frequency (f) and damping ratio (ξ) of the test models were discerned using the transfer function method. The half-power bandwidth method was utilized to determine the ξ value. The measuring point X9, Y9, Z15 were used as the output channels for the calculation of transfer functions to identify the vibration frequencies of the structure in different directions. The transfer function and damping ratio could be calculated:

$$G(\omega) = Y(\omega) / U(\omega) , \tag{2}$$

$$\xi = \Delta \overline{\omega} / 2 , \tag{3}$$

where ω is the circular frequency; $Y(\omega)$ and $U(\omega)$ represent the Fourier transformation of output value and input value, respectively; $\Delta \overline{\omega}$ is the half-power bandwidth.

The X- and Z-directional transfer function (TF) curves of the first white noise case are presented in Fig. 8. It's widely known that the rubber isolation bearings are mainly used to control the horizontal response of the structure, and compared with FB model, the first-order frequency of BI model was significantly reduced (see Fig. 8(a)). The first-order vertical vibration frequencies of BI model and FB model are 8.5 Hz and 8.8 Hz respectively (see Fig. 8(b)), and the first-order damping ratios are 0.35% and 0.36% respectively. The vertical fundamental frequency and damping ratio of FB and BI were very close, which indicates base isolation hardly changes the vertical dynamic characteristics of the grid layer. In order to delve deeper into the horizontal dynamic characteristics of the test models, as shown in Table 6, which presents the outcomes of four white noise excitations. The seismically isolated structure's superstructure primarily exhibits a flat vibration pattern, with deformation predominantly localized at the seismic isolation layer. Under condition W4-X, the BI model

Table 6. Horizontal Dynamic Characteristics of the Model

Condition	X-direction				Y-direction			
	f (Hz)		ξ (%)		f (Hz)		ξ (%)	
	BI	FB	BI	FB	BI	FB	BI	FB
W1	3.9	10.9	18.9	1.9	3.7	9.7	19.0	2.1
W2	3.8	10.7	19.3	2.2	3.6	9.7	19.1	2.2
W3	3.6	10.5	20.6	2.6	3.5	9.5	19.3	2.4
W4	3.3	10.0	21.9	3.1	3.2	9.1	19.6	2.9

demonstrated a damping ratio of 21.9% in the X direction, a significant increase compared to the 3.1% damping ratio observed in the FB model. A minimal variation in the fundamental frequency and damping ratio of both BI and FB from W1 to W4 suggests negligible structural damage. The first-order frequencies and damping ratios of the structure changed under the effect of four white noises. Overall, the damping ratios tend to slightly increase. Following multiple tests, it was observed that the horizontal frequency of the non-isolated structure remained largely unchanged. The base-isolation model exhibited damage primarily within the seismic isolation layer, while the superstructure remained largely undamaged, essentially in its elastic phase.

4. Experimental Results and Discussion

4.1 Influence of the Horizontal Seismic Component on the Vertical Response

In the stage of a 2D input rare intensity earthquake, the grid layer of the FB model had obvious vibration, indicating that the horizontal seismic component may also cause the vertical vibration of the whole or local structure. To clarify the magnitude of the vertical response caused by horizontal vibration and the impact of the coupling effect on the isolation effect, the responses of the structure and components measured under rare intensities are compared.

4.1.1 Vertical Acceleration Response of FB Structure

To derive the vertical oscillation instigated by the lateral seismic component, the vertical acceleration chronology of the measuring point P4 (refer to Fig. 6) within the FB model's grid stratum under the influence of 2D and 3D rare seismic inputs were compared, as depicted in Fig. 9. Under the horizontal input, the
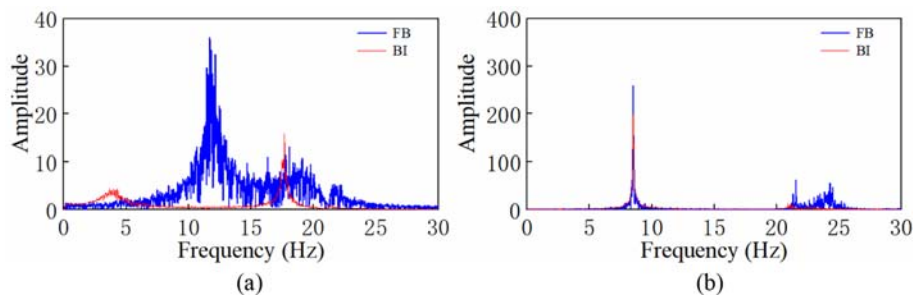

Fig. 8. Transfer Functions (TF) Curves of Test Models in Horizontal and Vertical Directions: (a) X Direction, (b) Z Direction
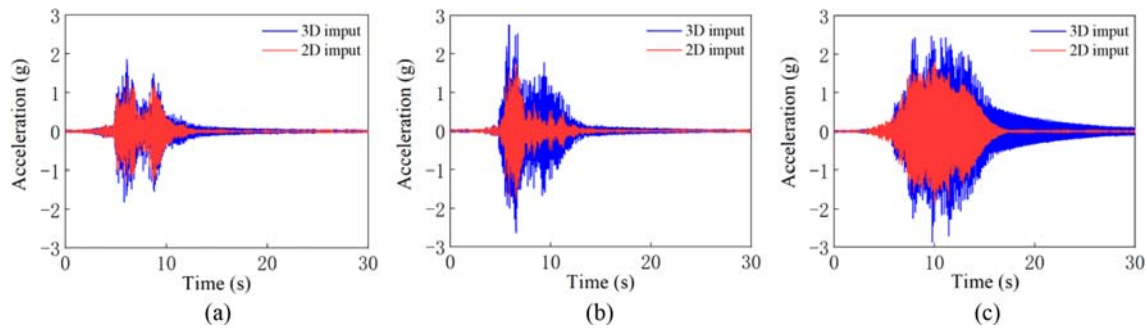
Fig. 9. Vertical Acceleration Time History of FB Model Grid: (a) El Centro Wave, (b) Taft Wave, (c) Artificial Wave

Table 7. Average Value of Peak Vertical Acceleration of FB Model Grid

Measuring Point	Vertical acceleration (g)		Ratio (2D/3D)
	2D input	3D input	
P1	1.439	2.140	0.67
P2	0.830	1.232	0.67
P3	1.610	2.526	0.64
P4	1.662	2.739	0.61
P5	0.965	2.268	0.43

grid layer had obvious vertical vibration, and the amplitude was more than half of the 3D input response. Under the 3D input El Centro wave, the peak vertical acceleration of the grid was 1.8 g, and under the 2D input, the peak reached 1 g. The two peaks under the 2D input wave were very close to those under the 3D input in time and size. This phenomenon proves that the vertical response caused by horizontal vibration cannot be ignored and is one of the main causes of the vertical response of the structure. The peak vertical acceleration under the 3D input Taft wave was 2.7 g, and the peak value under 2D excitation was 1.7 g. During the time domain with large acceleration response (4 s to 8 s), the change trend of the responses was similar. There was still an obvious vertical response under 2D excitation after the peak section, and the acceleration was maintained at approximately 0.5 g. An artificial record in accordance with the Chinese code response spectrum for 2% damping and soil classified as type II was selected as the seismic excitation for the shaking table test. Under artificial wave excitation, due to the longer peak time of seismic waves, the peak maintenance time of the structural

response was also longer than the other two wavelengths. From 5 s to 15 s, the change trend of acceleration under 2D and 3D excitation was basically the same. The trend indicates that in the vertical response under 3D excitation, the acceleration generated by the coupling effect accounts for a large proportion. The average peak values of vertical acceleration measured at five points are shown in Table 7. The comparison shows that the peak vertical acceleration caused by the 2D input earthquake reached more than 60% of the peak vertical acceleration caused by the 3D input earthquake, so the vertical response caused by horizontal vibration cannot be ignored.

4.1.2 Vertical Acceleration Response of BI Structure

The isolation layer composed of conventional lead-rubber bearings is considered to have no vertical isolation effect, and its vertical stiffness is typically less than the frame's vertical stiffness. The vertical acceleration time histories of the platform and the transfer layer under a 3D input earthquake are compared in Fig. 10. The peak acceleration of the vertical oscillation saw an increase of roughly 15% after traversing the isolation bearing. The comparison indicates that the isolation bearing does not provide a vertical damping effect, but rather an amplification effect.

To examine the vertical safeguarding of the isolation bearing on the infrastructure, the vertical acceleration time history of the P4 measuring point under 2D and 3D input earthquakes is contrasted in Fig. 11. As illustrated in Figs. 11(a) – 11(c), when exposed to the 2D seismic inputs, the peak acceleration of the BI model was less than 0.1 g, whereas the peak acceleration of the FB model exceeded 1 g. The vertical reaction of the isolated structure under lateral excitation was diminished by more than
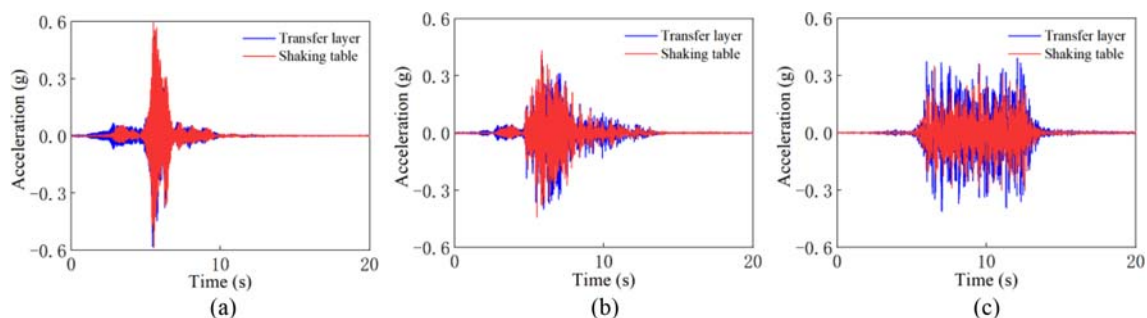

Fig. 10. Vertical Acceleration Time History of Shaking Table and Transfer Layer: (a) El Centro Wave, (b) Taft Wave, (c) Artificial Wave
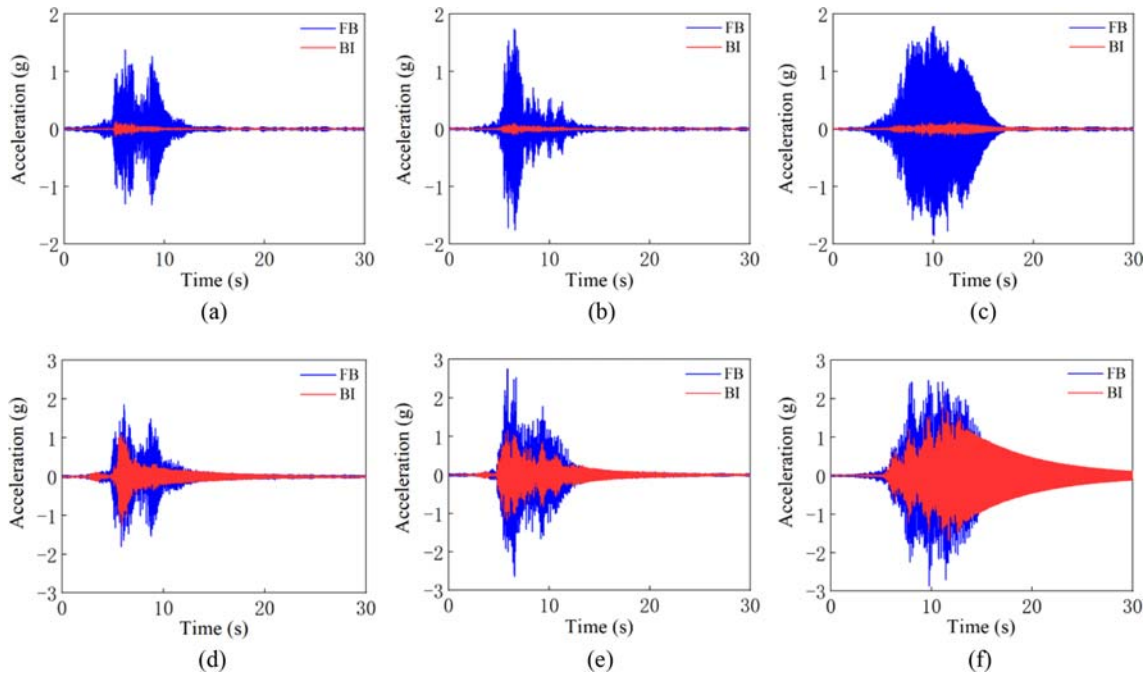
Fig. 11. Vertical Acceleration Time History of Grid: (a) El Centro Wave-2D, (b) Taft Wave-2D, (c) Artificial Wave-2D, (d) El Centro Wave-3D, (e) Taft Wave-3D, (f) Artificial Wave-3D

an order of magnitude. Since the vertical response under a 2D input earthquake was caused mainly by horizontal vibration through coupling, the isolation bearings had a good control effect on horizontal vibration, which greatly inhibited the horizontal vibration, and the vertical response caused by coupling was greatly reduced.

Under a 3D input earthquake, the acceleration of the BI model grid layer was also significantly reduced. As shown in Fig. 11(d), under the 3D input El Centro wave, the peak acceleration of the structure at approximately 8 s was reduced from 1.6 g in the FB model to 0.3 g in the BI model. Fig. 11(a) shows that under horizontal excitation, the FB model produced an acceleration response with a peak value of 1.3 g due to the coupling effect, and the isolated structure effectively inhibited the horizontal vibration, thereby increasing the period of the structure and reducing the acceleration response of the structure during the loading process. In Fig. 11(e), under the 3D input Taft wave, the peak value of the vertical response of the structure decreased from 2.7 g to 1 g after isolation. By observing the response of 4 s to 8 s under three-dimensional excitation, the response value was reduced from 1.5 g to 0.8 g, which was close to the time response value of the FB model under horizontal excitation in Fig. 11(b). As shown in Fig. 11(f), under a 3D artificial wave, the acceleration of grid was significantly reduced from 5 s to 15 s, and the peak value was reduced from 2.4 g to 1.5 g. Fig. 11(c) shows that the FB model grid did not produce obvious vertical response under horizontal excitation after 15 s, while the responses of the two models are basically the same after 15 s of 3D excitation in Fig. 11(f). This phenomenon also proves that the isolated structure has no control effect on the vertical excitation.

Table 8. Average Value of Peak Vertical Acceleration of Grid under 3D Seismic Excitation

Measuring Point	Vertical acceleration (g)		Ratio
	BI model	FB model	
P1	1.040	2.140	0.49
P2	0.837	1.232	0.68
P3	1.636	2.526	0.65
P4	1.361	2.739	0.50
P5	1.621	2.268	0.71

The mean values of the peak vertical acceleration reactions, triggered by three terrestrial movements of the BI and FB models, recorded at five points within the grid layer, are tabulated in Table 8. The acceleration magnitude of the BI model was roughly 60% of that of the FB model. Because of the horizontal isolation effect of base isolation, it effectively reduced the vertical vibration caused by horizontal-vertical coupling and the vertical isolation function was played.

4.1.3 Vertical Displacement Response

Figure 12 illustrates the time histories of vertical displacement for measuring point P5 (refer to Fig. 6) on the grid layer during rare earthquakes. It is evident from the Fig. 12 that the grid layer of both the BI and FB models experienced substantial vertical oscillations due to 3D input. In general, the vertical displacement amplitudes of BI model were less than that of FB model, suggesting that base isolation could reduce the vertical displacement response of the long-span roof when considering 3D seismic input. In
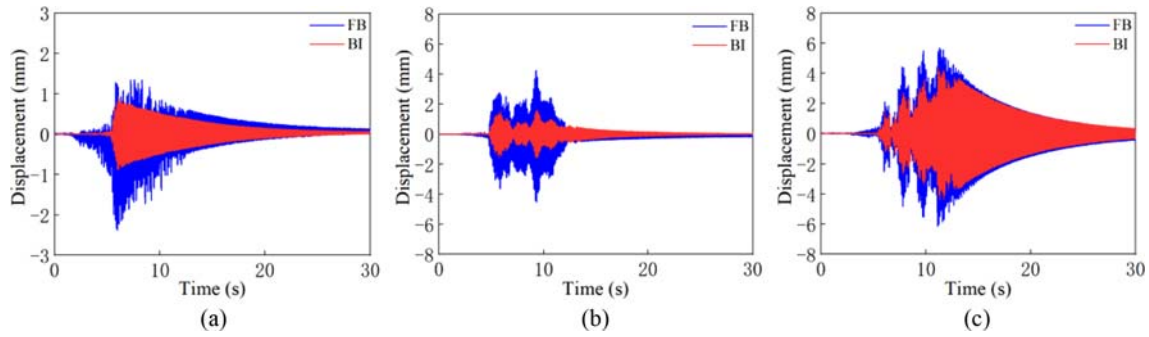
Fig. 12. Vertical Displacement Time History of Grid Roof: (a) El Centro Wave-3D, (b) Taft Wave-3D, (c) Artificial Wave-3D
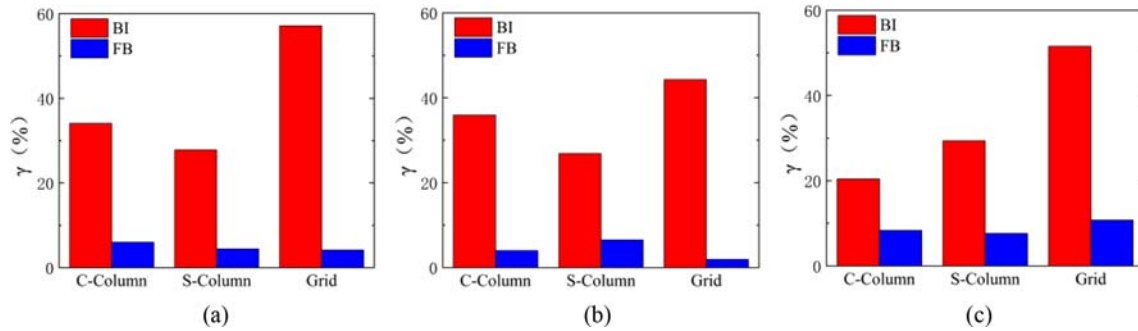

Fig. 13. Contribution Rate of Vertical Earthquake: (a) El Centro Wave, (b) Taft Wave, (c) Artificial Wave

Fig. 12(a) the response for the FB structure is strongly skewed towards negative displacements. This phenomenon is due to the displacement of the sensor caused during the test vibration, which could not be reset in time during the experiment. However, the trend in the data obtained from the monitoring is consistent with the trend obtained from the acceleration data monitoring.

Among the three ground motions, the El Centro wave induced the smallest amplitude of vertical vibration. As detailed in Section 2 that the period of vertical vibration was $1/f = 0.1176$ s ($f = 8.5$ Hz), the corresponding prototype period was 0.7438 s. As can be seen from Fig. 7(c), t it is evident that the vertical acceleration response spectrum value for this period of the El Centro wave was notably lower than the values for the other two waves, which accounts for the aforementioned observation. When subjected to 3D input from the Artificial wave, the BI and FB models exhibited greater vertical displacement amplitudes compared to those induced by the two natural seismic waves. However, the application of base isolation resulted in a reduction of the vertical displacement amplitude by more than 25%.

4.1.4 Strain Response of Grid

Xu et al. (2019) proposed a parameter, referred to as the contribution rate γ, to assess the impact of vertical earthquakes on component response. The definition of this parameter is as follows:

$$\gamma = (1 - \frac{\max(S_{2D}(t))}{\max(S_{3D}(t))}) \times 100\% , \qquad (4)$$

where S_{2D} and S_{3D} are the strain values measured under 2D and 3D input earthquakes, respectively.

In order to assess the coupling impact on the strain response

of components, measurements were taken at points located at the corner columns (B-Column, SG11), side columns (S-Column, SG7) and structural components (SG34), specifically under the conditions of rare earthquake intensity. The results of γ values calculated according to the formula are shown in Fig. 13. The γ values of the BI model were greater than the γ values of the FB model, indicating that the isolation bearings effectively inhibited the vertical response generated by coupling under horizontal earthquakes. In the FB model, the γ values are less than 10%, indicating that the vertical response caused by coupling in the FB model is greatly affected. In the BI model, average value of γ at the grid is about 50%, which reflects the contribution of vertical seismic excitation to the grid strain.

4.2 The Impact of the Vertical Seismic Component on the Horizontal Reaction

In the past tests (Griffith, 1988; Hwang and Hsu, 2000), in high-rise isolated structures, due to the coupling effect, the vertical excitation was found to have an amplification effect on the horizontal responses. In order to examine the coupling's impact on the horizontal responses of a long-span isolated structure, an analysis was conducted on the dynamic responses of both the superstructure and the isolation layer during rare earthquake events.

4.2.1 Amplification Effect of the Horizontal Acceleration

The lateral stiffness of the long-span structure grid layer is less than the lateral stiffness of the structure layer, and horizontal deformation occurs under earthquakes. In the experiment, the horizontal acceleration was amplified under three-dimensional
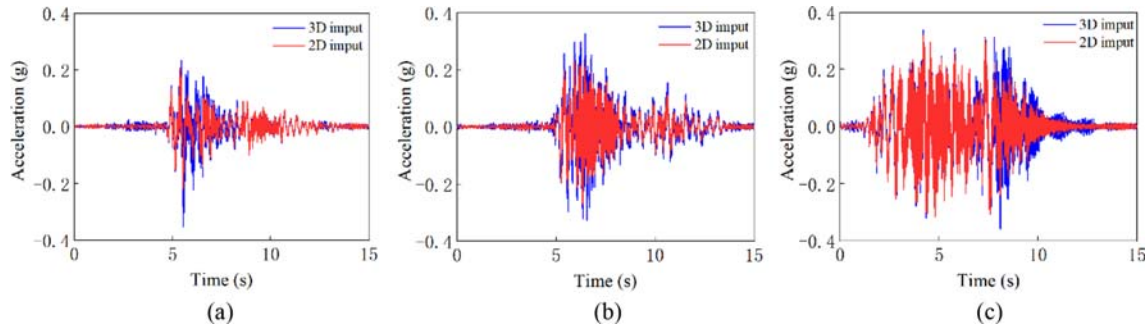
Fig. 14. Acceleration Time History in X Direction of BI Model Grid Layer: (a) El Centro Wave, (b) Taft Wave, (c) Artificial Wave
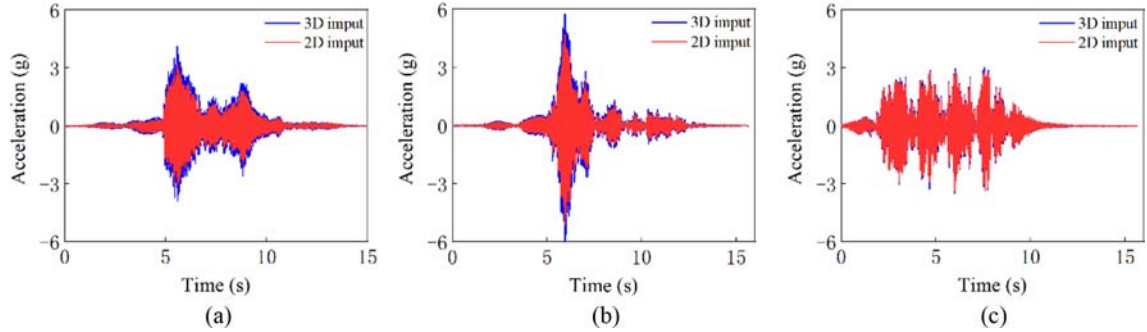

Fig. 15. Acceleration Time History in X-Direction of FB Model Grid Layer: (a) El Centro Wave, (b) Taft Wave, (c) Artificial Wave

excitation compared with the response under horizontal excitation. The horizontal accelerations on the grid X9 and Y8 of the BI model and FB model under three rare seismic waves are compared in Figs. 14 and 15.

To clarify the influence of the amplification on the isolation effect, the horizontal acceleration time histories of the BI model grid under 2D and 3D excitation are compared in Figs. 14(a) – 14(c). Figs. 14(a) and 14(b) show that the coupling amplification trends under the excitation of the El Centro wave and Taft wave were similar. In the peak sections of the El Centro wave (5 s – 7 s) and Taft wave (5 s – 8 s), the amplification of the horizontal response was obvious. In contrast to the Taft wave, the El Centro wave's peak acceleration experienced a significant increase, rising from 0.25 g and 0.2 g to 0.4 g and 0.35 g respectively, nearly doubling in magnitude. Figs. 14(c) and 15(c) show that, unlike the data almost fitted in the FB model, the horizontal acceleration of the BI model had a significant amplification for a long time after 7 s. When subjected to artificial wave excitation, the BI model's horizontal acceleration time history under 3D seismic excitation demonstrated noticeable amplification, but the peak horizontal acceleration of the BI model was still below 0.4 g after amplification by the coupling effect. By observing the response of the FB model, the peak values were all above 3 g, and the responses were reduced by nearly 10 times to a reasonable range.

Compared with the BI model, the acceleration amplification effect of the grid in the FB model was not obvious. As shown in Fig. 15(a), the horizontal response under 3D input was generally greater than the horizontal response under 2D input in the whole process of El Centro wave action, and the amplification effect

was the most obvious at the peak acceleration stage. Under 2D excitation, the peak acceleration was 3 g, while under 3D excitation, the peak acceleration reached 4 g. In Fig. 15(b), under the action of the Taft wave, the amplification trend was the same as the amplification trend under the El Centro wave. Amplification is most obvious in the peak part, and the peak increases from 4 g to 6 g. As shown in Fig. 15(c), the acceleration response under 3D excitation of artificial waves is basically consistent with the amplification trend under two-dimensional excitation, but the amplification trend still increases in some periods. The comparison showed that the increase in acceleration in the FB model was not obvious, but the increase was much larger than the increase in acceleration in the BI model, indicating that compared with the non-isolated structure, the vertical seismic component increases the horizontal acceleration of the isolated structure more significantly. Therefore, appropriate consideration should be given to the magnification effect of vertical earthquakes when designing large-span seismic isolation structures.

The acceleration time history of the grid layer indicates that the coupling of horizontal and vertical vibrations led to an amplification of the horizontal responses. In order to examine the impact of this horizontal-vertical coupling on the overall structure's response, a comparison was made of the average peak acceleration recorded by each floor, as shown in Fig. 16. Although horizontal acceleration peak amplification occurred in each layer, the amplification was most obvious in the grid layer. Table 9 indicates the grid layer's horizontal peak acceleration responses under severe earthquake excitations, and the peak acceleration amplification factor (AF) of 3D excitation compared with 2D excitation was analysed for calculating the growth rate. The results showed that
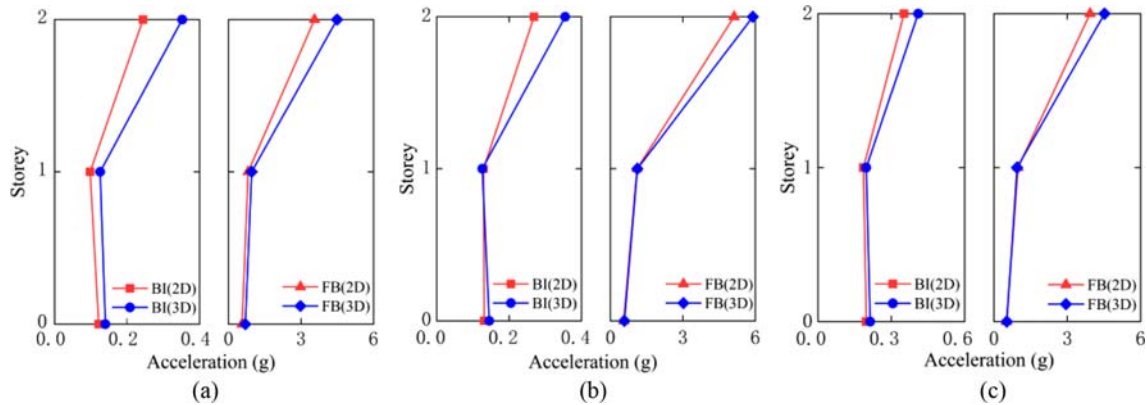
Fig. 16. Peak Floor Acceleration in X-Direction: (a) El Centro Wave, (b) Taft Wave, (c) Artificial Wave

Table 9. Horizontal Peak Acceleration of Grid Layer under Rare Earthquake

Model	Seismic wave	Acceleration (g)		Growth rate (%)
		2D input	3D input	
FB	El Centro	3.55	4.49	26.48
	Taft	5.12	5.89	15.04
	Artificial	3.93	4.52	15.01
BI	El Centro	0.24	0.35	45.83
	Taft	0.27	0.35	29.63
	Artificial	0.35	0.41	17.14

the AFs are greater under the action of the El Centro waves and the Taft waves, which was consistent with the phenomenon observed in Fig. 16. As shown in Figs. 14 and 15, under the excitation of the two natural waves, the amplification occurred mainly in the peak section. Under artificial waves, the amplification of the FB model was not obvious, and the amplification of the BI model response time history was concentrated mainly after the peak. By comparing Figs. 14 and 15, the amplification effect of coupling on horizontal acceleration in the BI model was found to be more obvious than the amplification effect of coupling on horizontal acceleration in the FB model. According to the data of Table 9, the amplification effect of horizontal acceleration induced by horizontal-vertical interaction is significant both for FB and

BI models and the growth rate of the BI model under 3D input is higher than that of FB model, but the peak acceleration of each floor in the BI model is much smaller. Therefore, it can be concluded that although the vertical seismic action significantly intensifies the horizontal seismic response, the mitigation effect of the BI model in the horizontal direction is undoubtedly very superior.

4.2.2 Dynamic Behaviour of the Isolation Layer

In addition to the structural response, the coupling effect also appears in the mechanical behaviour of the isolation bearing.

Figure 17 illustrates the trajectory of horizontal displacement for the bearing, as recorded by the DX1 and DY1 displacement sensors under both 2D and 3D input. The peak displacement values for the bearing can be found in Table 10. The trajectory of the isolation bearing under 3D input was similar to the trajectory of the isolation bearing under 2D input, but there was obvious deviation and amplification under 3D input. As shown in Figs. 17(a) and 17(b), under 3D input El Centro and Taft wave excitation, the trajectory envelope curves were enlarged compared with the trajectory envelope curves under 2D input excitation. Under artificial wave excitation (Fig. 17(c)), the displacement time history curves were approximately linear due to the same seismic signals in two horizontal directions. Compared with the horizontal trajectory, only the boundary points had obvious offsets, and they were more obvious in the X-direction. As shown in Fig. 17(c), the X-direction offset of the boundary point reached
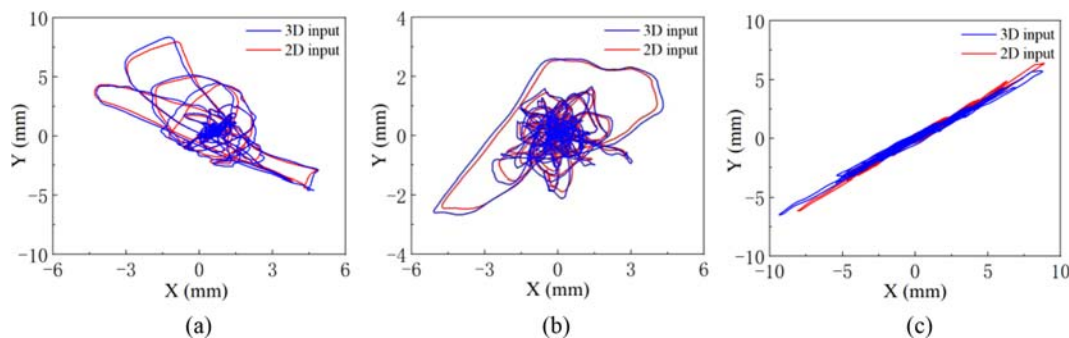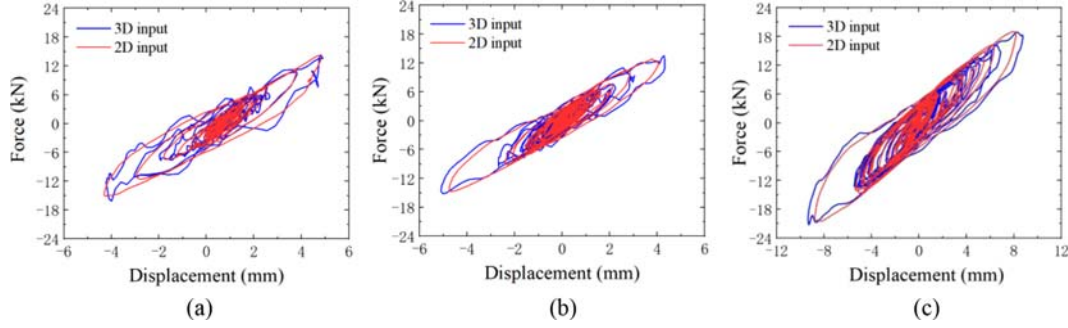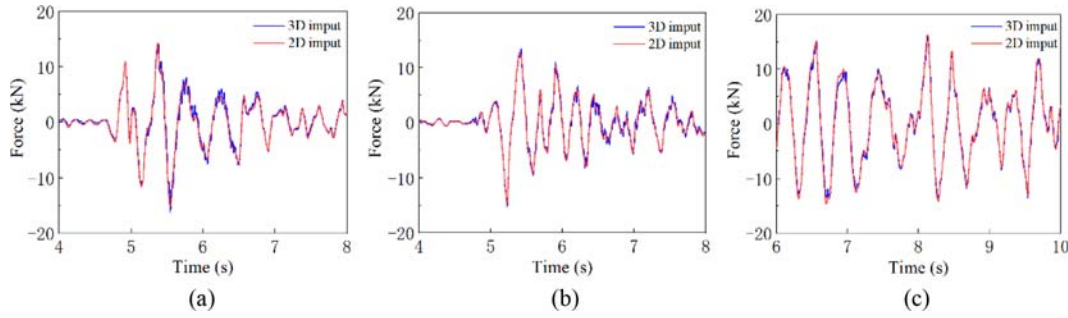

Fig. 17. Horizontal Displacement Curve of Isolation Layer: (a) El Centro Wave, (b) Taft Wave, (c) Artificial Wave

Table 10. Maximum Horizontal Displacement of Isolation Layer

Wave	Maximum X displacement (mm)		Growth rate (%)	Maximum coupling displacement (mm)		Growth rate (%)
	2D input	3D input		2D input	3D input	
El Centro	4.83	4.89	1.24	8.01	8.45	5.49
Taft	4.75	5.10	8.09	5.06	5.71	7.33
Artificial	8.79	9.35	6.37	11.02	11.39	3.36
Mean	6.12	6.45	6.81	8.12	8.52	4.93

Fig. 18. X-Direction Hysteresis Curve of Isolation Layer: (a) El Centro Wave, (b) Taft Wave, (c) Artificial Wave

Fig. 19. Horizontal Shear Force Time History of Isolation Layer: (a) El Centro Wave, (b) Taft Wave, (c) Artificial Wave

1.3 mm. Table 10 shows that although the track curve of the bearing has visible amplification offset, the maximum displacement amplification is not obvious.

To further study the coupling effect on the isolation bearings, Fig. 18 presents a comparison of the hysteretic curves of the isolation layer in the X-direction under both 2D and 3D earthquake inputs. These hysteresis curves serve as a reflection of the motion state and energy dissipation of the isolation bearing during an earthquake. The shear time history can be derived by multiplying the mass of the floor with the acceleration time history recorded by the corresponding floor. The maximum shear force of the ith floor can be estimated by summing the inertial force time, as outlined in Eq. (5).

$$F_i(t)_{max} = \left| -\sum_{j=i}^{n} m_j a_j(t) \right|_{max}, \qquad (5)$$

where $F_i(t)_{max}$ is the maximum inter-story shear force of story i; m_j and $a_j(t)$ are the mass and the measured acceleration time history of story j, respectively; n is the total number of layers.

Figure 18 illustrates that the hysteresis curves under 3D input

exhibit minor fluctuations when contrasted with 2D input, particularly during the El Centro wave excitation. The time histories of the X-direction shear force of the isolation layer within a specific time domain are depicted in Fig. 19, where a notable oscillation in the horizontal shear force is observed. Additionally, the oscillation amplitude under El Centro wave excitation was comparable to that under other two ground motions. Abe et al. (2004a, 2004b) conducted the experimental and theoretical research on the multi-axial mechanical properties of LRBs, and found that horizontal restoring force of LRB is significantly affected by the value of the vertical load. The vertical inertia force of the superstructure was calculated using the measured vertical acceleration, and the vertical seismic force time history of the isolation layer is shown in Fig. 20. It can be seen that there was almost no vertical response for the BI model under 2D seismic input. When compared with the other two ground motions, the El Centro wave induced the most substantial variation in the vertical seismic force of the seismic isolation layer. This implies that the LRBs are subjected to considerable fluctuations in axial pressures. Based on the findings presented in literatures (Abe et al., 2004a, Abe et al., 2004b), the horizontal
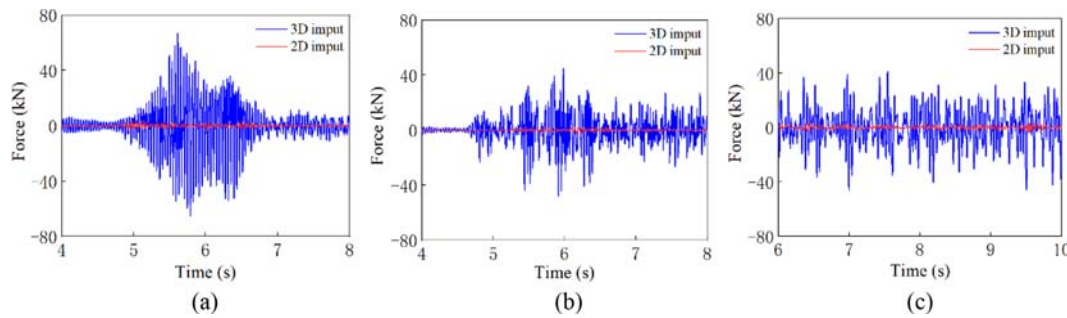
Fig. 20. Vertical Force Time History of Isolation Layer: (a) El Centro Wave, (b) Taft Wave, (c) Artificial Wave

mechanical behaviour of the LRBs would change due to the varying axial pressures, which also explains the reason for oscillation of hysteretic curves of isolation layer under 3D input, and the oscillation was the most significant under El Centro wave excitation.

5. Numerical Simulation

In view of the shaking table test model made more simplifications, especially the grid part, the test results cannot reflect the dynamic response caused by some complex-high-order vibration modes. Therefore, the dynamic response and parameter influence analysis were carried out in the numerical analysis on the prototype structure and the following numerical investigation mainly focuses on the BI structure.

5.1 Numerical Verification of Shaking-Table Test
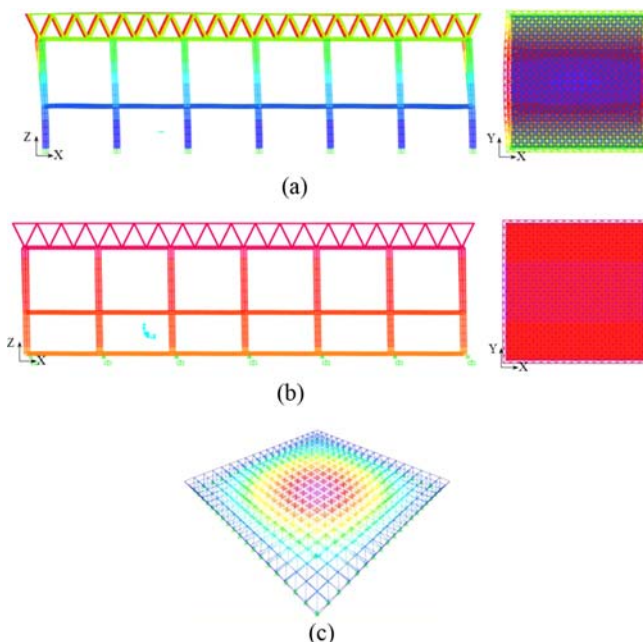The prototype structure's numerical model was established

Fig. 21. Vibration Mode Diagram of Numerical Model: (a) X-Directional First-Order Vibration Mode of FB Structure, (b) X-Directional First-Order Vibration Mode of BI Structure, (c) Z-Directional First-Order Vibration Mode of Gird Roof

utilizing SAP2000 finite element software. Its accuracy and the validity of the numerical modeling method were confirmed by comparing it with test results. Both numerical models underwent vibration mode analysis and dynamic time-history response analysis. Fig. 21 displays the first-order modes in the X- and Z-directions of the numerical models. It can be seen from Fig. 21(a) that the vibration shape of the FB structure exhibits shear deformation, and the deformation at the top layer of the beam is greater because the stiffness is lower than that of the frame layer. Fig. 21(b) shows that the superstructure of the BI structure nearly rigid body without relative deformation, and horizontal deformation is concentrated in the seismic isolation layer with very low lateral stiffness. Fig. 21(c) gives the first-order vertical vibration of the gird roof, with the deformation gradually increasing from the periphery to the center. The comparison between the horizontal frequencies of the FEM results and the experimental models are presented in Table 11. The prototype structure exhibits a vertical frequency of 1.21 Hz, while the scaled structure's measured frequency stands at 1.34 Hz, marking a discrepancy of 9.70%. A comparative analysis reveals a fundamental alignment in the dynamic characteristics of the test and numerical models. However, certain deviations emerge between the test results and numerical analysis due to modeling simplifications, such as the impact of welds on stiffness and the assumption of ideal boundary conditions.

The displacements of the seismically isolated structure are concentrated in the seismic isolation layer under the earthquake, and Table 12 shows the horizontal displacement of the seismic isolation layer under the rare earthquake action. The comparisons of vertical acceleration are presented in Table 13, the errors of peak acceleration of measurement points P2 and P5 are almost within 20%. By comparing the acceleration response and the seismic

Table 11. Natural Frequency of Numerical Model Compared with the Test Model

Model	Mode	Frequency (Hz)			Error (%)
		Test value	Conversion value	Numerical value	
FB	X direction	10.90	1.72	1.38	19.77
	Y direction	9.70	1.53	1.38	9.80
BI	X direction	3.90	0.62	0.61	1.71
	Y direction	3.70	0.58	0.61	-3.60

Table 12. Comparison of Displacement of Isolation Layer between Test and Numerical Results

Direction	Ground motion	Maximum displacement (mm)			Error (%)
		Test value	Conversion value	Numerical value	
	El Centro wave	4.83	193.20	191.63	-0.81
X	Taft wave	4.45	178.00	145.14	-18.46
	Artificial wave	8.87	354.80	330.13	-6.95
	El Centro wave	7.95	318.00	324.54	2.06
Y	Taft wave	2.58	103.20	97.93	-5.11
	Artificial wave	6.39	255.60	280.21	9.63

Note: Error = (Numerical value − Conversion value) / Conversion value

Table 13. Comparison of Vertical Acceleration of Test and Numerical Results

Measuring Point	Ground motion	Maximum acceleration (g)		Error (%)
		Test value	Numerical value	
	El Centro wave	1.171	1.289	10.08
P2	Taft wave	0.691	0.690	-0.14
	Artificial wave	0.648	0.622	-4.01
	El Centro wave	1.321	1.182	-10.52
P5	Taft wave	1.434	1.468	2.37
	Artificial wave	1.909	1.491	-21.90

Note: Error = (Numerical value − Test value) / Test value

isolation layer's displacement from both the numerical model and the experimental data, it is found that the discrepancies are within an acceptable range. Consequently, the numerical model proves to be both precise and dependable.

5.2 Numerical Analysis Results

5.2.1 Influence of Yield-to-Weight Ratio

The yield-to-weight ratio α is the ratio of the total yield force of the seismic isolation layer to the total weight above the isolation layer, which is a key parameter in seismic isolation design (Providakis, 2008; Xie et al., 2021). The isolation layer's total yield force can be modulated by altering the lead core's diameter in the LRB, thereby adjusting the isolation layer's yield-to-weight ratio, denoted as α. Seismic response characteristics of BI structure with 11 yield-to-weight ratios of 0%, 1%, 2%, 3%, 4%, 5%, 6%, 7%, 8%, 9%, and 10%, were investigated, and the influence of the yield-to-weight ratios on the important seismic isolation design indexes (seismic isolation coefficient and displacement of the isolation layer for large earthquakes) and vertical acceleration at long-spam roof were analyzed. Fig. 22 illustrates the influence of α on both the seismic isolation coefficient and the isolation layer's horizontal displacement for a long-span isolated structure. This is observed under the impact of three seismic waves corresponding to an 8-degree rare earthquake. As shown in Fig. 22(a), the seismic isolation coefficient of the BI structure generally increases with the increase of the yield-to-weight ratio under the action of three seismic waves with 8-degree rare earthquake, and a smaller seismic isolation coefficient could be obtained when the yield-to-weight ratio was 1% − 3%. As the yield-to-weight ratio escalates, there is a corresponding decline in the displacement of the isolation layer. Taking into account the seismic isolation effect and deformation control of the seismic isolation layer, the yield-to-weight ratio of 2% − 3% was appropriate.

Figure 23 shows the relationship between the vertical acceleration at gird roof and the yield-to-weight ratio. Under the influence of 2D seismic input, the grid's vertical acceleration saw a swift increase with the rise in yield-to-weight ratio. However, the peak acceleration remained notably minimal, registering less than one-tenth of that observed under 3D input, as shown in Fig. 23(a). Fig. 23(b) shows that the influence of yield-to-weight ratio on the vertical acceleration of the structure was slight. This phenomenon is explained as follows: As the yield-to-weight ratio increases, there is a corresponding gradual increase in the vertical acceleration response triggered by the horizontal seismic component. The BI structure's grid primarily responds to the vertical seismic component, with the yield-to-weight ratio alterations having negligible impact
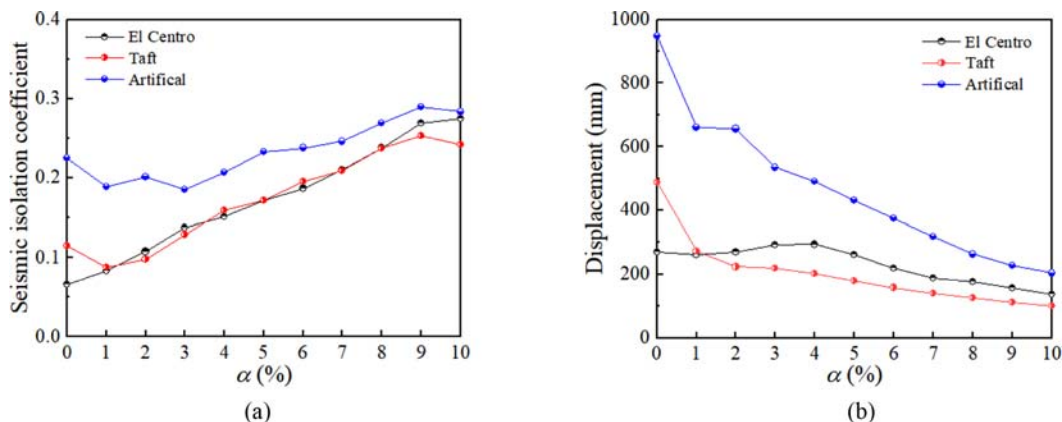
Fig. 22. Seismic Isolation Coefficient and Horizontal Displacement of the Isolation Layer for the Large-Span Isolated Structure with Different Yield-to-Weight Ratios: (a) Seismic Isolation Coefficient, (b) Displacement of Isolation Layer
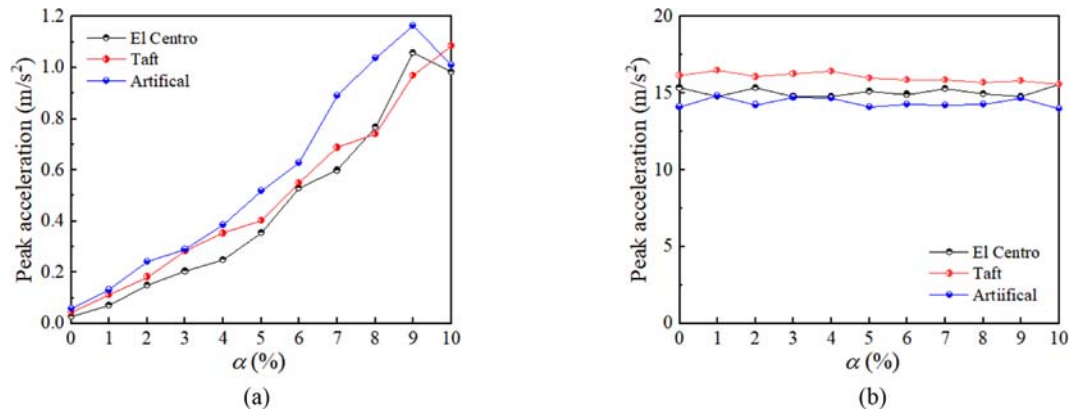
Fig. 23. Vertical Peak Acceleration of the Center Point of Long-Span Gird Roof with Different Yield to Weight Ratios: (a) 2D Input, (b) 3D Input
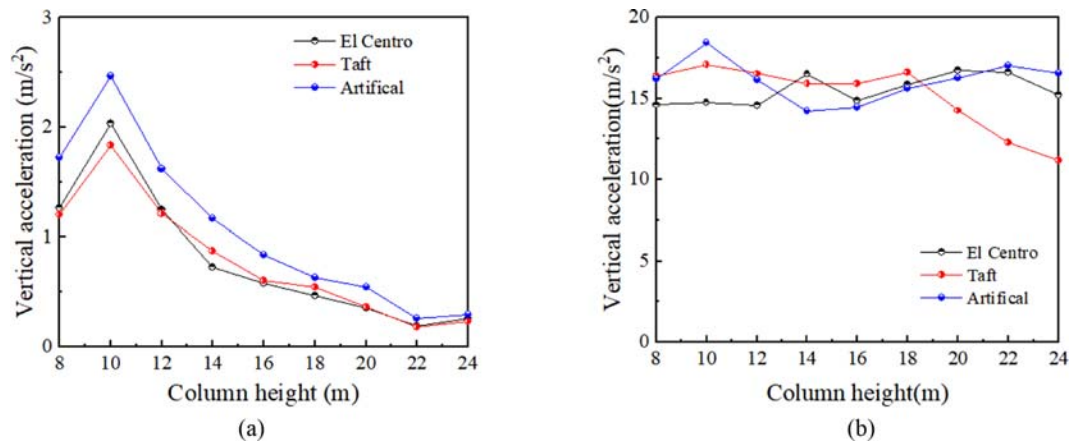

Fig. 24. Vertical Peak Acceleration of the Center Point of Long-Span Gird Roof with Different Height of Gird Layer: (a) 2D Input, (b) 3D Input

on the seismic isolation layer's vertical mechanical attributes.

5.2.2 Influence of Column Height of Roof Layer

For the long-span spatial structures, the column height of gird layer is the supporting height of the long-span roof, which is an important factor in determining the lateral stiffness of the gird roof. The dynamic response analysis of BI structures with different supporting height of roof layer under 2D and 3D seismic input with rare earthquake intensity was performed. Vertical peak acceleration of the center point of long-span gird roof The variation trend of vertical peak acceleration of the center point of long-span gird roof with different supporting heights in Fig. 24. It is observed that, with 2D seismic input, the vertical peak acceleration decreased with the increase of the supporting height (see Fig. 24(a)). With 3D seismic input, the peak acceleration of the grid with different supporting heights under different seismic wave excitations shows different trends, but, in general, the peak fluctuated around 15 m/s².

In general, as the support height increased, the horizontal stiffness of the roof layer decreased and the peak horizontal acceleration increased and then decreased. The peak horizontal acceleration under 3D seismic input was basically larger than that under 2D input, as shown in Fig. 25.
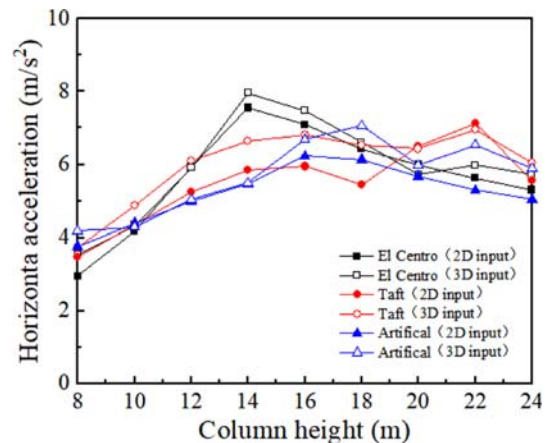

Fig. 25. Horizontal Acceleration of Grid Roof with Different Column Height of Gird Layer

5.2.3 Peak Vertical Acceleration Distribution of Grids

The vertical acceleration response has a significant effect on the non-structural members, such as suspended ceilings. It is beneficial to clarify the acceleration peak distribution to guide the location optimization and design the connection between the non-structural members and structural members. Fig. 25 illustrates the cloud diagram depicting the peak vertical acceleration of the grid when
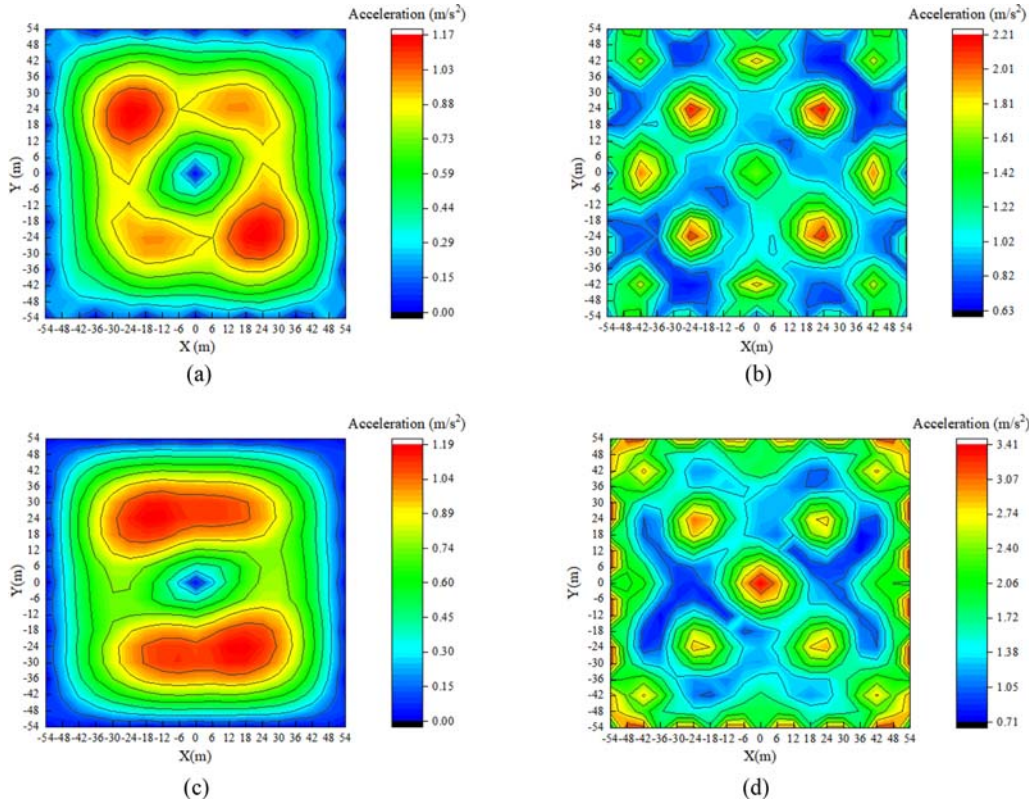
Fig. 26. Vertical Peak Acceleration Distribution of Grid Roof Under Frequent Earthquake: (a) FB Structure with 2D Input, (b) FB Structure with 3D Input, (c) BI Structure with 2D Input, (d) BI Structure with 3D Input
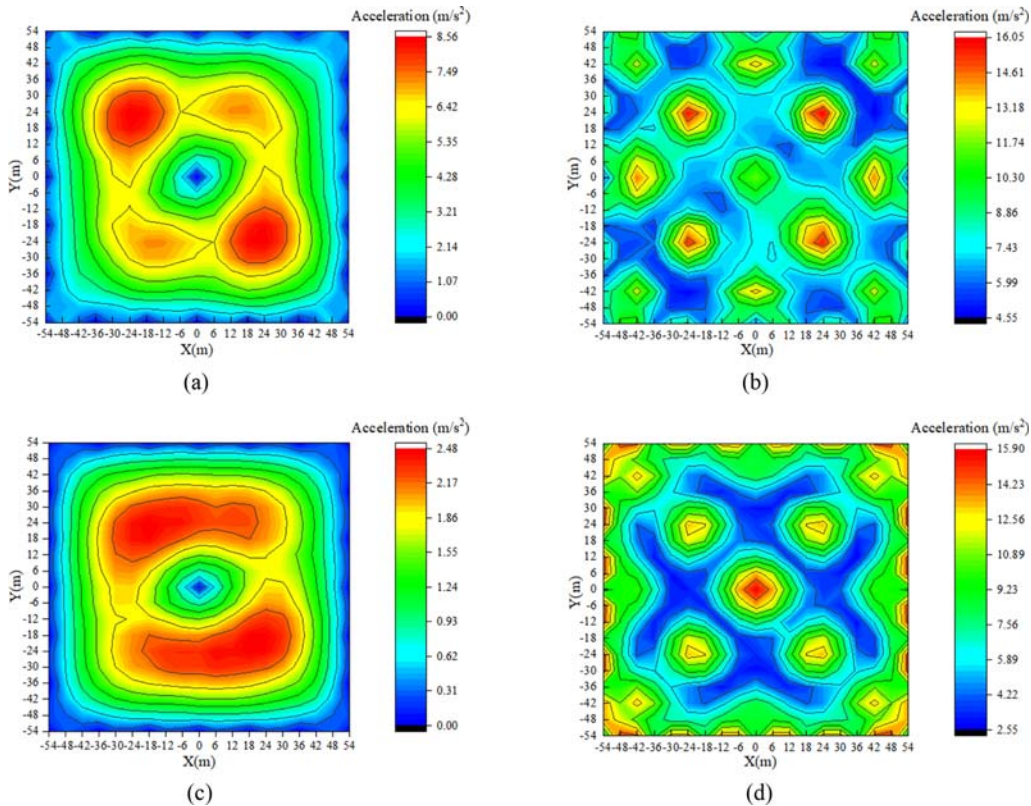

Fig. 27. Vertical Peak Acceleration Distribution of Grid Roof Under Rare Earthquake: (a) FB Structure with 2D Input, (b) FB Structure with 3D Input, (c) BI Structure with 2D Input, (d) BI Structure with 3D Input

subjected to the El Centro wave excitation, with a PGA of 110 cm/s², characteristic of a frequent earthquake. The vertical peak values of both FB and BI structures under 3D seismic input were larger than that under 2D seismic input, and the distribution pattern also had a large difference. Fig. 26 illustrates that under 2D seismic input, the FB structure's peak vertical acceleration is observed in the upper left and lower right areas of the grid plane. This is attributed to the cumulative effect of the vertical dynamic response triggered by seismic components from various directions. The vertical maximum acceleration of the BI structure under the 2D seismic input appears above and below the grid plane, whereas the maximum vertical acceleration of the grid was distributed on the diagonal of the grid plane and around when subjected to 3D seismic excitation.

Figure 27 presents the distribution of the grid's peak vertical acceleration under the influence of a rarely earthquake. The BI structure's peak vertical acceleration is less than a third of the FB structure's under 2D seismic input, signifying that base isolation can notably diminish the grid's acceleration coupling effect during rare earthquakes. The peak acceleration of the BI structure with 3D seismic input was significantly larger than that with 2D seismic input, and acceleration peak distribution pattern was similar to that under frequent earthquake. Therefore, if possible, some important equipment installed on the roof should avoid placement in the area of high vertical acceleration response on the roof or enhance the strength of the connections of non-structural members in this area.

6. Conclusions

This research examined the impact of horizontal-vertical vibration interaction on long-span isolated structures using a 1:40 scale model of a typical long-span steel frame, both with and without base isolation. The dynamic responses, including acceleration, displacement, and strain, of the two test models under 2D and 3D seismic inputs were documented. The study analyzed the test data to understand the influence of horizontal vibration on the vertical response of long-span isolation structures and the vertical seismic effect of isolation bearings. Furthermore, the study evaluated the impact of coupling amplification on the horizontal isolation effect. The primary conclusions drawn from the analysis of the test results are as follows:

1. The comparison results of the vertical acceleration time history response of the grid roof of the FB model under 2D and 3D earthquakes show that the time period for the vertical acceleration to reach the peak is similar. Furthermore, the peak vertical acceleration of grid roof of FB model induced by horizontal seismic excitation reached 60% of that caused by 3D excitation, indicating that the horizontal earthquake has a significant influence on the vertical response of the grid layer of the fixed-base structure.

2. Compared with FB model, the peak vertical acceleration of grid layer in BI model subjected to 3D excitation was reduced by 40%. Although the LRBs applied to the long-span roof structure cannot supress the vertical vibration induced by vertical ground motion, they can effectively attenuate the vertical vibration of the grid roof caused by coupling in the base-isolated structure by reducing the horizontal response.

3. When considering the vertical seismic excitation, the horizontal acceleration response of the BI model grid layer was increased by 30%, indicating that the vertical vibration amplifies the horizontal response of the base-isolated structure to a certain extent. Under 2D and 3D seismic excitations, the horizontal peak acceleration of the BI model was approximately 1/10 of that of the FB model. It can be seen that, compared to fixed-base structure, even considering the horizontal-vertical coupling of earthquakes, the horizontal seismic isolation effect of base-isolated structures is still very excellent.

4. Compared with the structural responses under 2D excitation, the maximum displacement of the isolation layer of the test model under 3D excitation was increased by about 5.3%. In addition, due to the influence of the axial force, the horizontal mechanical behaviour of isolation bearings had changed, resulting in a slight oscillation of the horizontal shear force. It is recommended that the effect of horizontal-vertical coupling on the deformation and shear behaviour of isolation bearings should be considered.

5. Numerical models accurately reflect the dynamic behavior of test models, indicating that a yield-to-weight ratio of 2% to 3% achieves favorable horizontal seismic isolation effects while minimizing isolation deformation in long-span BI structures. Lowering the support height reduces the horizontal acceleration response of the grid layer under 3D seismic excitation, with minimal impact on the vertical acceleration. It is notable that the maximum acceleration of grids in FB and BI structures occurs at different locations and should be considered when designing the arrangement or connection of non-structural members for large-span roofs.

It should be noted that the study of the coupling effect of horizontal and vertical excitations is important to guide the design of large-span BI structures and the arrangement or connection of non-structural members at the roof. However, due to the small scaled factor (1/40), the prototype structure and the test structure have different second-order effects, and cannot fully reflect all the dynamic properties of the prototype structure. Therefore, it makes sense to carry out further tests on large-span structures with slightly larger scaling factor or to refine the simulation of prototype structures. In addition, the effect of near-fault earthquakes on the dynamic response of large-span isolated structures still needed further study.

Acknowledgments

ORCID

Tianyang Zhang ⓘ https://orcid.org/0009-0004-4454-8112
Yunlong Zhang ⓘ https://orcid.org/0009-0000-5408-5490
Weizhi Xu ⓘ https://orcid.org/0000-0001-8040-0335

References

Abe M, Yoshida J, Fujino Y (2004a) Multiaxial behaviors of laminated rubber bearings and their modeling. I: Experimental study. *Journal of Structural Engineering* 130(8):1119-1132, DOI: 10.1061/(ASCE)0733-9445(2004)130:8(1119)

Abe M, Yoshida J, Fujino Y (2004b) Multiaxial behaviors of laminated rubber bearings and their modeling. II: Modeling. *Journal of Structural Engineering* 130(8):1133-1144, DOI: 10.1061/(ASCE)0733-9445(2004)130:8(1133)

Anand V, Kumar SR (2018) Seismic soil-structure interaction: A state-of-the-art review. *Structures* 16:317-326, DOI: 10.1016/j.istruc. 2018.10.009

China Ministry of Housing and Urban-Rural Development (2010) Code for seismic design of buildings. GB 50011-2010. China Architecture and Industry Press (in Chinese)

Clough R, Penzien J (1975) Dynamics of structures. McGraw-Hill, New York, NY, USA, 27-46

Computer & Structures Inc (2015) CSI analysis reference manual for SAP2000, ETABS. Berkeley, California, USA, 14-59

Ding YL, Chen X, Li AQ, Zuo XB (2011) A new isolation device using shape memory alloy and its application for long-span structures. *Earthquake Engineering and Engineering Vibration* 2:239-252, DOI: 10.1007/s11803-011-0062-4

Ding JM, Chen CJ, Wu HL (2019) Recent application and key issues of isolation technology in large-span complex buildings. *Journal of Building Structures* 40(11):1-10, DOI: 10.14006/j.jzjgxb.2018.0394 (in Chinese)

Furukawa S, Sato E, Shi YD (2013) Full-scale shaking table test of a base-isolated medical facility subjected to vertical motions. *Earthquake Engineering and Structural Dynamics* 42(13):1931-1949, DOI: 10.1002/eqe.2305

Griffith MC (1988) Experimental evaluation of seismic isolation of medium-rise structures subject to Uplift. Report No. UCB-EERC 88-02, University of California: Berkeley, CA, USA

Hu K, Jiang L, Qu G (2016) Study on design method of isolation buildings and engineering application. *Journal of Building Structures* 46(S1): 434-438, DOI: 10.19701/j.jzjg.2016.s1.092 (in Chinese)

Huffmann GK (1985) Full base isolation for earthquake protection by helical springs and viscodampers. *Nuclear Engineering and Design* 84(3):331-338, DOI: 10.1016/0029-5493(85)90246-8

Hwang JS, Hsu TY (2000) Experimental study of isolated building under triaxial ground excitations. *Journal of Structural Engineering* 126(8):879-886, DOI: 10.1061/(ASCE)0733-9445(2000)126:8(879)

Jung JW, Kim MK, Kim JH (2022) Experimental study on the floor responses of a base-isolated frame structure via shaking table tests. *Engeering Structures* 253:113763, DOI: 10.1016/j.engstruct.2021. 113763

Kunnath SK, Erduran E, Chai YH, Yashinsky M (2008) Effect of near-fault vertical ground motions on seismic response of highway overcrossings. *Journal of Bridge Engineering* 13(3):282-290, DOI: 10.1061/(ASCE)1084-0702(2008)13:3(282)

Lu WD, Liu WQ, Wu XF (2011) Shaking table test of terminal a structure of kunming international airport. *Journal of Building Structures* 6:27-33, DOI: 10.14006/j.jzjgxb.2011.06.010 (in Chinese)

Mazza F, Mazza M, Vulcano A (2018) Base-isolation systems for the seismic retrofitting of R.C. framed buildings with soft-storey subjected to near-fault earthquakes. *Soil Dynamics and Earthquake Engineering* 109:209-221, DOI: 10.1016/j.soildyn.2018.02.025

Mazza F, Vulcano A (2012) Effects of near-fault ground motions on the nonlinear dynamic response of base-isolated R.C. framed buildings. *Earthquake Engineering and Structural Dynamics* 41(2):211-232, DOI: 10.1002/eqe.1126

Mazza F, Vulcano A, Mazza M (2017) Nonlinear response of r.c. framed buildings retrofitted by different base-isolation systems under horizontal and vertical components of near-fault earthquakes. *Earthquakes and Structures* 12(1):135-144, DOI: 10.12989/eas.2017.12.1.135

Papazoglou AJ, Elnashai AS (1996) Analytical and field evidence of the damaging effect of vertical earthquake ground motion. *Earthquake Engineering and Structural Dynamics* 25(10):1109-1137, DOI: 10.1002/(SICI)1096-9845

Providakis CP (2008) Effect of LRB isolators and supplemental viscous dampers on seismic isolated buildings under near-fault excitations. *Engineering Structures* 30(5):1187-1198, DOI: 10.1016/j.engstruct. 2007.07.020

Ryan KL, Dao ND (2012a) NEES/E-Defense base-isolation tests: Interaction of horizontal and vertical response. 15th World Conference on Earthquake Engineering, September 24-28, Lisbon, Portugal

Ryan KL, Warn PG (2012b) A review of seismic isolation for buildings: Historical development and research needs. *Buildings* 2(3):300-325, DOI: 10.3390/buildings2030300

Shu WN, Zhu ZY, Qi Y (2016) Design and research on terminal building of Beijing New Airport. *Journal of Building Structures* 46(17):1-7, DOI: 10.19701/j.jzjg.2016.17.001 (in Chinese)

State General Administration of the People's Republic of China for Quality Supervision and Inspection and Quarantine (2007) Rubber bearings Part 1: Test methods for isolation rubber bearings. GB/T20688.1-2007. China National Standardization Administration Committee Press (in Chinese)

Takahashi O, Aida H, Suhara J, Matsumoto R (2008a) Construction of civil building using three dimensional seismic isolation system (Part 1, Design of Building Using Three Dimensional Seismic Isolation System). 14th World Conference on Earthquake Engineering, October 12-17, Beijing, China

Takahashi O, Aida H, Suhara J, Matsumoto R (2008b) Construction of civil building using three dimensional seismic isolation system (Part 2, Tests for Three Dimensional Seismic Isolation System). 14th World Conference on Earthquake Engineering, October 12-17, Beijing, China

Takeuchi T, Xue SD, Kato S (2006) Recent development in passive control technologies for mental spatial structures. Extended Abstracts of International Symposium on New Olympics New Shell and Spatial Structures, Beijing, China

Tubino F, Carassale LG, Solari G (2003) Seismic response of multi-supported structures by proper orthogonal decomposition. *Earthquake Engineering and Structural Dynamics* 32(9):1639-1654, DOI: 10.1002/eqe.292

Victor AZ, Stanley SL (2000) Seismic isolation for strong, near-field earthquake motions. 12th World Conference on Earthquake Engineering, January 30-February 4, Silverstream, Upper Hutt, New Zealand

Xie LL, Yan HY, Zeng DM (2021) Research on the influence of the yield ratio on existing RC frame-shear wall structures retrofitted by seismic isolation. *Building Science* 37(3):145-150, DOI: 10.13614/j.cnki.11-1962/tu.2021.03.023 (in Chinese)

Xu WZ, Du DS, Wang SG, Liu WQ, Li WW (2019) Shaking table tests on the multi-dimensional seismic response of long-span grid structure with base-isolation. *Engeering Structures* 201(201), DOI: 10.1016/j.engstruct.2019.109802

Xue SD, Li XY, Pan KJ (2010) Seismic isolation technology application in spatial structures. *Journal of Building Structures* A2:56-6, DOI: 10.14006/j.jzjgxb.2010.s2.056 (in Chinese)

Yoshiro O, Kawaguchi K, Shunji O (2008) Damage to non-structural components in large roof buildings failed during the Iwate-Miyagi Nairiku earthquake in 2008 or an earthquake in the north shore of Iwate prefecture in July 24th of 2008. *AIJ Journal of Technology and Design* 16(33):821-826, DOI: 10.3130/aijt.16.821

Zhu HP, Zhou FY, Yuan Y (2014) Development and analysis of the research on base isolated structures. *Engineering Mechanics* 31(3):1-10, DOI: 10.6052/j.issn.1000-4750.2013.05.ST05 (in Chinese)